Ethane Cation-radical Isomers and their Interconversion Pathways. Electron Shift Isomerism in Cation Radicals

Alexander Ioffe†,[a] **and Sason Shaik** *,[b],‡
[a] *The Department of Chemistry, Ben-Gurion University, Beer-Sheva 84105, Israel*
[b] *The Department of Organic Chemistry and The Fritz Haber Center of Molecular Dynamics, The Hebrew University, 91904 Jerusalem, Israel*

An extensive computational exploration of the $C_2H_6^{+\cdot}$ surface has been performed with electron correlation methods beyond MP2, up to the level of quadratic configuration interaction with single, double and triple substitutions, using the 6-311G** basis set. Five ground-state species, two excited-state species and five transition states, for interconversions and internal rotations, are located. The results at the highest levels show the existence of three isomers, which in order of decreasing stability are: ^2A_g $(C_{2h})_{DB}$, $^2A_{1g}$ (D_{3d}) and $^2A''$ (C_s), where the most stable isomer has a diboranoid (DB) character. Two interconversion pathways are found to link the diboranoid ^2A_g $(C_{2h})_{DB}$ isomer to the other two isomers. The lowest energy mechanism appears to be the one linking ^2A_g $(C_{2h})_{DB}$ and $^2A_{1g}$ (D_{3d}). Thus, the work identifies a low-energy mechanism which funnels the dynamics through the original point-group symmetry, away from the traditional Jahn–Teller pathway. Each event of $^2A_{1g}$ (D_{3d}) formation is, in turn, followed by a faster reverse process back to ^2A_g $(C_{2h})_{DB}$ which results in scrambling of the hydrogens in the bridging positions. These results offer the basis for an interpretation of the observed EPR spectrum (reference 8) in the low-as well as the high-temperature studies. A qualitative analysis of the origins of the various isomers and their interconversion pathways is presented. It is shown that a useful way of understanding the results is in terms of 'electron-shift isomerism' in which single electron-shifts amongst different fragments of the atomic skeleton generate both the $C_2H_6^{+\cdot}$ isomers as well as their intervening transition structures.

The electronic and three-dimensional structures of the isomers of ethane cation-radicals[1–5] have been, in recent years, a source of controversy and discrepancy as yet unresolved, between theory and experiment. The origins and nature of the controversy can be discussed by reference to Fig. 1 which shows the frontier orbitals of ethane and the corresponding vertical states of $C_2H_6^{+\cdot}$, $^2A_{1g}$ and ^2E_g, which are generated by electron loss from these orbitals.

The first discrepancy is related to the question of whether it is the $^2A_{1g}$ or the ^2E_g state that corresponds to the first band maximum in the low-energy part of the photoelectron (PE) spectrum of ethane.[4,5] Straightforward use of the Koopmans' theorem,[6] to resolve the assignment of the maxima, is unreliable because of the extreme closeness of the $3a_{1g}$ and $1e_g$ orbitals which inhibits the band assignment even at higher theoretical levels. Thus, Hartree–Fock theory predicts a $^2A_{1g}$ ground state,[1,5e] while correlated computational levels seem, albeit not always, to favour a ^2E_g ground state, as may be deduced by comparing the configuration interaction (CI) results of Buenker, Peyerimhoff and collaborators[5c] with the Green's function calculations of Cederbaum *et al.*[5d] and with the Møller–Plesset (MP)[7] perturbation theoretical calculations by Radom *et al.*[1]

The second discrepancy is related to the adiabatic isomers of $C_2H_6^{+\cdot}$. The majority of previous calculations indicated that the most stable isomer is the $^2A_{1g}$ state which derives from the corresponding vertical state by C–C bond elongation, and which preserves thereby the original D_{3d} point-group symmetry. This structure possesses six equivalent hydrogens with almost zero spin density,[1,2] and is therefore inconsistent with the low-temperature EPR spectrum (taken at 4.2 K in an SF_6 matrix) which was reported by Iwasaki and collaborators.[8] The spectrum was found to exhibit a 1:2:1 three-line hyperfine splitting with a coupling constant of *ca.* 150 G, which corresponds to a structure belonging to a C_{2h} point-group

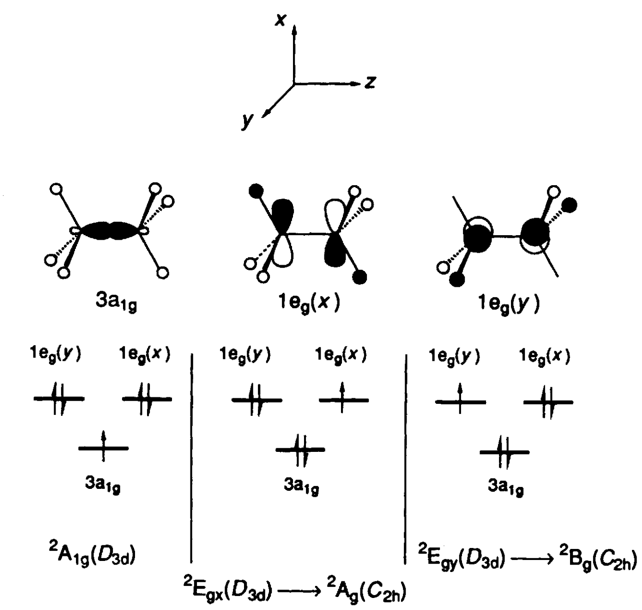

Fig. 1 The vertical states of $C_2H_6^{+\cdot}$ obtained by electron ionization from the frontier orbitals $3a_{1g}$ and $1e_g$ which are drawn above the configurations. The components of $1e_g$ are designated by parenthetical *x* and *y* to signify the orientations of the p AOs in the molecular coordinate system. The point-group symmetries of the vertical and the expected adiabatic states are indicated below the corresponding configurations.

* Correspondence should be addressed to the Department of Organic Chemistry, Philadelphia Building. The Hebrew University, 91904 Jerusalem, Israel.
† Current address is at BGU
‡ On leave from BGU. The former name is Sason S. Shaik.

symmetry and having a high concentration of spin density on two of the six hydrogens (0.6 of the total spin).[8] It remained however inconclusive as to whether this EPR emitting species is also the ground state of $C_2H_6^{+\bullet}$ or whether it is a deformed species constrained in the cavity of the SF_6 matrix.[2,8] A recent MP2/6-31G** study by Lunel and Huang[3] shows that the ground state of $C_2H_6^{+\bullet}$ is indeed a ^2A_g (C_{2h}) isomer which is more stable than $^2A_{1g}$ (D_{3d}) by *ca.* 0.35 kcal mol^{-1}, and which possesses diboranoid character with two bridging hydrogens, as well as isotropic hyperfine constants in good agreement with the low-temperature EPR spectrum. The part of the story yet to be addressed belongs to the high temperature ($\geqslant$ 77 K) EPR spectrum which shows seven equally spaced lines with 50 G spacing, which now indicate six equivalent hydrogens with significant spin density (*ca.* 0.1 spin on each H). This is again inconsistent with the $^2A_{1g}$ (D_{3d}) species, but may reflect the dynamic behaviour of the ^2A_g (C_{2h}) isomer.[8] What is the precise nature of this dynamic behaviour of the diboranoid structure and what are its origins and relationship to the vertical ^2E_g parent state (Fig. 1)? What is the role played by the $^2A_{1g}$ (D_{3d}) structure? Is this latter structure a computational artifact, or does it have a role in the dynamics of $C_2H_6^{+\bullet}$?

Other related and unresolved structural questions are those concerning the status of the ^2B_g (C_{2h}) and $^2A''$ (C_s) isomers which derive from the Jahn–Teller-active ^2E_g vertical state. Bellville and Bauld found, by means of MNDO calculations, a structure that fits the $^2A''$ (C_s) description but did not report its exact details.[2] Radom *et al.*[1] located the two structures at the 3-21G level and found $^2A''$ (C_s) to be more stable than ^2B_g (C_{2h}), but their stability order was shown to be the reverse by single-point calculations at the MP3/6-31G*//HF/6-31G* level. The order reversal together with the findings of two imaginary frequencies for ^2B_g (C_{2h}) and a single one for $^2A''$ (C_s) cast doubt on the status of these species. Thus, the jigsaw puzzle is incomplete, and the resulting pictures are still not clear, both in terms of the potential-energy surface as well as the related Jahn–Teller behaviour of $C_2H_6^{+\bullet}$.

In this present paper we try to complete the jigsaw puzzle by an extensive and high-level computational exploration of the $C_2H_6^{+\bullet}$ surface, coupled with qualitative curve-crossing and configuration-mixing analyses of the isomers and their interconversion transition states.[9,10] The results at the highest computational levels establish the existence of three isomers: the diboranoid structure ^2A_g (C_{2h}), an ethane-like $^2A_{1g}$ (D_{3d}) isomer and an electronically localized $^2A''$ (C_s) structure. The most stable isomer is found to be the diboranoid structure ^2A_g (C_{2h}) which is connected to the other two isomers by corresponding transition structures. All high-computational levels lead to the same conclusion that the lower-energy pathway is the one that links ^2A_g (C_{2h}) and $^2A_{1g}$ (D_{3d}) and *which thereby funnels the dynamics through the original point-group symmetry, away from the traditional Jahn–Teller dynamics.* This mechanism leads to scrambling of the bridging positions and provides a simple rationale for the EPR observations in the high-temperature studies. As will be shown, a useful way of understanding the various $C_2H_6^{+\bullet}$ isomers as well as their connecting transition states, is *via* their interrelations by means of single electron-shifts amongst different fragments of the atomic skeleton. We refer to this structural variety as 'electron-shift isomerism'.

Theoretical Methods and Calculations

All computations were performed with the GAUSSIAN-90 and GAUSSIAN-92 series of programs[11,12] on IBM/RS6000 Workstations at Ben-Gurion University and the Hebrew University. The notation used to qualify the computational level is standard,[13] *e.g.*, MP4 = Full/6-311G**//MP2 = Full/6-311G** stands for a single point calculation on the MP2 = Full/6-311G** optimized geometry with correlation corrections at the MP4 approximation on the same basis set. The qualification 'Full' of the post-SCF options refers to the inclusion of core orbitals in the correlation treatment. The lack of this qualification means, in turn, the use of frozen-core approximation.

The geometries of C_2H_6, its cation-radicals and their interconversion transition states were optimized by gradient methods and checked by frequency calculations using 6-31G* and 6-311G**[14] basis sets at the restricted (RHF or RMP2 for C_2H_6) and unrestricted (UHF and UMP2 for $C_2H_6^{+\bullet}$) optimization levels, with the highest uniform level being MP2 = Full/6-311G**//MP2 = Full/6-311G**. The pathways which connect the various isomers *via* corresponding transition states were ascertained by use of IRC options.

For the principal isomers, the geometry optimization was carried out by post-SCF levels more complex than MP2. These correlated levels used for the advanced optimization are: 4th order Møller–Plesset correction (UMP4 and MP4)[15], configuration interaction with double substitutions (CID)[16] as well as with single and double substitution (CISD)[16], coupled-cluster calculations with double substitutions (CCD),[17] coupled-cluster calculations involving single- and triple-excitation correction through fourth order using the CCD wavefunction (ST4CCD),[18] and quadratic CI involving singles, doubles as well as triples [QCISD,[19] QCISD(T)[19]]. MCSCF calculations[20] were performed for the $^2A_{1g}$ (D_{3d}) isomer within the a_{1g} orbital manifold of the 6-31G* basis set.[21] At all these latter levels, the Berny optimization procedure[22] was used.

Calculated vibrational frequencies and entropies were used (wherever appropriate) to evaluate thermodynamic contributions to relative energies of the isomers and the transition states in order to ascertain the existence of separating barriers in a thermochemical sense. The calculated frequencies were not scaled since the MP2 frequencies are generally believed not to need scaling.[13]

Vertical ionization potentials [E_i(v)] were obtained as the differences in electron energies of the neutral C_2H_6 and of its corresponding cation-radical, both calculations being performed at the optimum geometry of the neutral. In the calculations of adiabatic ionization potentials [E_i(a)], the cation-radical was allowed to relax to its optimum geometry. The E_i(a) values were calculated also at the ΔH° scale by inclusion of thermal energy corrections.

Results

A compilation of structures and energies is given in the Appendix to this paper.

Geometries and Energies of C_2H_6 *and* $C_2H_6^{+\bullet}$ *Isomers.*—Following Radom *et al.*[1] the cation-radicals were generated by subtracting one electron, in turn, from each one of the frontier orbitals $3a_{1g}$ and $1e_g$ (Fig. 1) and optimizing the structures for the resulting $^2A_{1g}$, $^2E_{gx}$ and $^2E_{gy}$ electronic configurations. Following the same routine, two excited states arising from the ^2E_u configurations were generated by subtracting one electron from the degenerate $1e_u$ MOs which are related to $1e_g$ as simply their bonding combinations. The MP2 = Full/6-311G**//MP2 = Full/6-311G** optimized structures of the neutral parent (**a**) and the cation-radical isomers (**e**–**h**) are depicted in Fig. 2 in order of decreasing stability with the computed relative energies (in kcal mol^{-1})* indicated in

* 1 cal = 4.184 J.

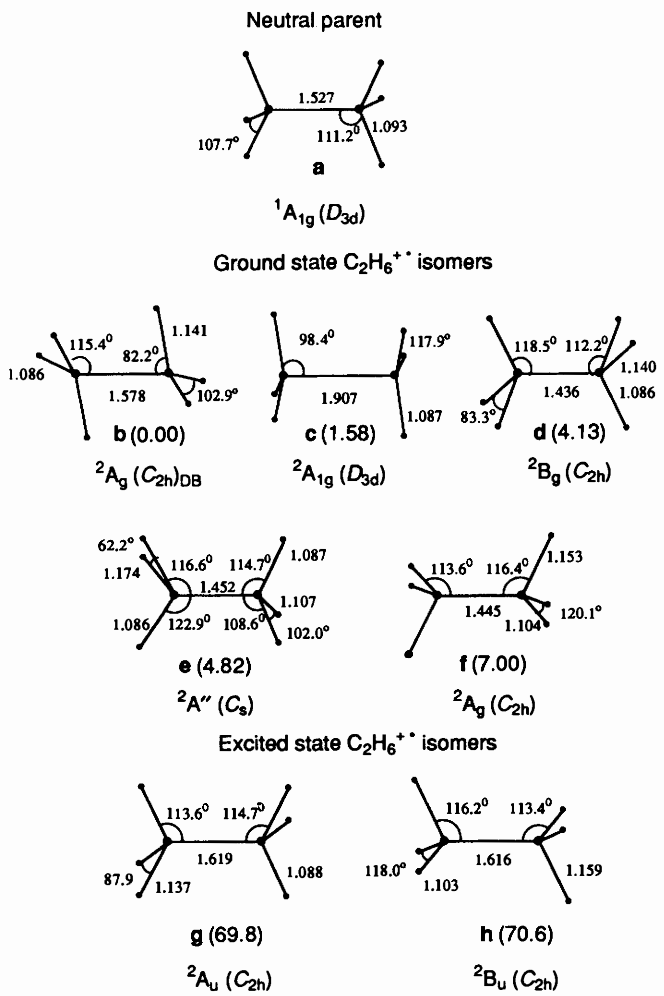

Fig. 2 Optimized geometries of C_2H_6 and $C_2H_6^{+\bullet}$ isomers. Relative energies for the isomers of the cation-radicals are shown in parentheses (in kcal mol^{-1}). Geometry and relative-energy data are at the MP2 = Full/6-311G**//MP2 = Full/6-311G** level.

parentheses. In Table 1 are collected the pertinent data on three different levels of geometry optimization.

The two excited states in Fig. 2 derive from Jahn–Teller unstable ^2E_u configurations which relax to the C_{2h} point group and give rise to the ^2A_u (**g**) and ^2B_u (**h**) adiabatic excited states. These states are seen to lie *ca.* 70 kcal mol^{-1} (*ca.* 3 eV) higher than the most stable isomer (**b**), in good accord with the ^2E_u − $^2A_{1g}/^2E_g$ energy differences reported in the PE spectrum.[5a] The structural characteristics of these excited states are in accord with the loss of C–C bonding character upon ionization from the $1e_u$ MOs. Thus, the two states involve longer C–C bonds (*ca.* 1.62 Å) in comparison with the neutral parent molecule.

Let us turn now to the ground state isomers of $C_2H_6^{+\bullet}$. The optimized structure of the $^2A_{1g}$ isomer (**c**) conserves the original D_{3d} symmetry, but has a much longer C–C bond and a smaller in-plane HCC angle, in comparison with the neutral parent, as might be expected from the character of the $3a_{1g}$ MO (Fig. 1). On the other hand, the isomers derived from the Jahn–Teller unstable ^2E_g configuration, break the original D_{3d} symmetry, but in a more subtle way than the expected simple orbital description of Jahn–Teller behaviour, and giving rise thereby to four isomers indicated as **b**, **d**, **e** and **f** in Fig. 2. Isomers **d** and **f** behave in accord with the simple orbital picture. Thus, the ^2B_g (C_{2h}) isomer (**d**) possesses a shortened C–C bond and smaller HCH angles, relative to the neutral parent, in accord with ionization from the $1e_{gy}$ component of the degenerate MO pair. Similarly, species **f** corresponds to ionization from the $1e_{gx}$ MO and possesses the expected shortened C–C bond and elongated in-plane C–H bonds and wide in-plane HCC angle. However, this wide-angled ^2A_g (C_{2h}) structure is not a real minimum and possesses two imaginary frequencies.

The other two isomers (**b** and **e**) are also derived from the ^2E_g configurations but do not behave in the expected manner from the simple orbital picture. Thus, the $^2A''$ (C_s) isomer, **e** is a version of ^2B_g (C_{2h}), but one in which the ionization is localized in one of the CH_2 groups instead of in both groups as in **d**.[1,2] The ^2A_g (C_{2h})$_{DB}$ isomer (**b**), with elongated C–C and C–H bonds and with an in-plane HCC angle of 88.2°, deviates further from the simple orbital picture and does not correspond in a straightforward way to an ionization from any particular orbital of the original $1e_g$ set. This isomer is the diboranoid (DB) structure characterized by Lunel and Huang,[3] and is accordingly designated hereafter by the subscript DB.

As may be seen from Fig. 2, the ground surface of $C_2H_6^{+\bullet}$ is soft and involves four minima, which are condensed in energy, well within a range of 5 kcal mol^{-1}. While these results are quantitatively as well as qualitatively different from previous results,[1–3] the data in Table 1 show that they may not represent the final picture. Thus, the diboranoid isomer ^2A_g (C_{2h})$_{DB}$ exists only at correlated levels but is not always the most stable isomer, while the $^2A''$ (C_s) isomer seems to require a high-quality basis set to be a real minimum. This unstable behaviour highlights the need to upgrade the computational level.

Table 2 shows the energies and structural features of the two most stable electron-shift isomers, ^2A_g (C_{2h})$_{DB}$ and $^2A_{1g}$ (D_{3d}), at different computational levels, the highest of which, in the sense of total energy, is the QCISD(T)/6-311G** optimization level (entries 15 and 26). It is seen that while the D_{3d} isomer is a true minimum at all the levels, the diboranoid isomer oscillates, though at the highest levels its existence seems to be a stable fact. The structural features of the two isomers exhibit similar trends, in the sense that while the C–C bond length of the D_{3d} isomer converges at the highest levels to 1.915 Å (entries 13–15), the same bond length in the diboranoid isomer defines a range of 1.65–1.74 Å (entries 23–26). The same is true for the C–H bond lengths of the bridging hydrogens in the diboranoid structure which cluster in the range 1.112–1.130 Å. This is an indication of the softness of the surface near the diboranoid structure rather than any major flaw in—or unreliability of—the computational levels.

Let us turn now to the ^2B_g (C_{2h}) and $^2A''$ (C_s) structures which coexist as minima on the MP2 = Full/6-311G** optimization level. These two isomers are mutually related as delocalized and localized forms of the same species (see later the spin density distribution in **5** and **6**). From previous experience with similar problems,[23] it appeared that localized and delocalized forms of the same species are generally mutually exclusive and therefore ^2B_g (C_{2h}) and $^2A''$ (C_s) may not coexist as true minima. In order to test the relative stabilities of the 'localized' structure and the 'delocalized' one, we have constructed a transformation coordinate, ΔR, which is equal to the difference in C–H bond length in the two CH_2 moieties. The values for this coordinate are 0.0673 Å for the $^2A''$ structure and precisely zero for the ^2B_g structure. The structure was then varied by stepping at intervals of 0.005 Å along the transformation coordinate while optimizing all other parameters, at each computational level, and constructing thereby the energy profiles shown in Fig. 3. The profiles exhibit a gradual change from two minima on the MP2/6-311G**/MP2/6-311G** level to a single minimum at the QCISD(T)/6-311G**/MP2/6-311G** level. At this highest level, only the $^2A''$ isomer survives as a minimum, while the delocalized structure lies *ca.* 1.3 kcal mol^{-1} higher in energy and serves as a transition state between two equivalent and mirror image $^2A''$ (C_s) structures.

In Table 3 are collected the relative energies of the four species

Table 1 Total energies [a] and optimized geometries of C_2H_6 and its adiabatic $C_2H_6^{+\bullet}$ isomers [b]

	Optimization level		
	MP2 = Full/6-311G**	HF/6-311G**	MP2 = Full/6-31G*
(a) $^1A_{1g}$ (D_{3d})			
Electronic energy, H/p	−79.608 59	−79.251 71	−79.503 97
R C–C/Å	1.527 0	1.526 7	1.524 6
R C–H/Å	1.092 9	1.086 2	1.092 9
<C–C–H/deg	111.15	111.20	111.19
(b) ^2A_g (C_{2h})$_{DB}$			
Electronic energy, H/p	−79.184 07	Does not exist	−79.084 77
$\langle S^2\rangle$ [c]	0.762		0.760
R C–C/Å	1.577 2		1.549 6
R C–H/Å	1.141 0		1.148 3
R C–H_2/Å	1.086 4		1.087 4
<C–C–H/deg	82.20		85.11
<C–C–H_2/deg	115.44		116.16
dihedral angle H–C–H [d]	140.0		140.0
(c) $^2A_{1g}$ (D_{3d})			
Electronic energy, H/p	−79.181 56	−78.875 84	−79.084 79
$\langle S^2\rangle$ [c]	0.760	0.759	0.758
R C–C/Å	1.906 5	1.961 2	1.918 8
R C–H/Å	1.087 2	1.077 0	1.086 7
<C–C–H/Ådeg	98.38	98.42	98.60
(d) ^2B_g (C_{2h})			
Electronic energy, H/p	−79.177 49	−78.834 83	−79.079 56
$\langle S^2\rangle$ [c]	0.770	0.770	0.766
R C–C/Å	1.436 1	1.423 8	1.436 6
R C–H/Å	1.085 9	1.076 4	1.086 9
R C–H_2/Å	1.139 6	1.137 1	1.139 9
<C–C–H/deg	118.51	118.65	117.84
<C–C–H_2/deg	112.24	112.13	112.08
Dihedral angle H–C–H [d]	91.7	92.3	96.8
(e) $^2A''$ (C_s)			
Electronic energy, H/p	−79.176 39	−78.848 20	Does not exist
$\langle S^2\rangle$ [c]	0.758	0.757	
R C–C/Å	1.451 5	1.477 8	
R C–H/Å	1.085 8	1.076 7	
R C–H_2/Å	1.174 0	1.172 8	
R C–H′/Å [e]	1.086 9	1.080 0	
R C–H_2′/Å [e]	1.107 3	1.089 9	
<C–C–H/deg	122.89	123.24	
<C–C–H_2/deg	116.58	117.53	
<C–C–H′/deg [e]	114.74	113.05	
<C–C–H_2′/deg [e]	108.59	108.39	
Dihedral angle H–C–H [d]	70.5	67.1	
Dihedral angle H–C–H′ [d,e]	110.0	115.0	
(f) ^2A_g(C_{2h}) [f]			
Electronic energy, H/p	−79.172 97	Does not exist	Does not exist
$\langle S^2\rangle$ [c]	0.772		
R C–C/Å	1.444 7		
R C–H/Å	1.153 2		
R C–H_2/Å	1.103 9		
<C–C–H/deg	116.36		
<C–C–H_2/deg	113.64		
Dihedral angle H–C–H [d]	142.0		

[a] Total energies are reported in Hartree/particle (H/p). [b] The letters **a**–**f** alongside the species correspond to the designations in Fig. 2. [c] $\langle S^2\rangle$ before annihilation of unwanted spin states. After annihilation, $\langle S^2\rangle$ is always 0.750. [d] Angle H–C–H in the corresponding Newman projection. [e] Bond lengths and angles in the less perturbed part of the molecule—see structure in Fig. 2. [f] Not a true minimum—two negative frequencies.

on a few of the highest computational levels. The first group of three entries gives the energy difference using single-point calculations on the MP2 = Full/6-311G** optimized geometry, while the second group of six entries includes the highest internally consistent levels (energy and geometry optimizations on the same level) in which the isomers coexist as true minima. The highest levels, except for ST4CCD, show that the diboranoid structure is the most stable isomer of $C_2H_6^{+\bullet}$ by *ca.* 0.3–1.6 kcal mol^{-1} relative to the $^2A_{1g}$ (D_{3g}) isomer, and 5–6 kcal mol^{-1} relative to $^2A''$ (C_s) and ^2B_g (C_{2h}). At the highest levels the ^2B_g (C_{2h}) isomer is the least stable, and according to Fig. 3, this isomer is likely to be a transition structure rather than a minimum.

Ionization Potentials.—Having identified $^2A_{1g}$ (D_{3d}) and ^2A_g (C_{2h})$_{DB}$ as the two most stable isomers of $C_2H_6^{+\bullet}$ it is possible

Table 2 Optimized structures of the $^2A_{1g}$ (D_{3d}) and ^2A_g (C_{2h})$_{DB}$ isomers of $C_2H_6^{+\bullet}$[a]

(c) $^2A_{1g}$ (D_{3d}) Entry	Optimization Level	Electronic energy (Hartree/particle)	$\langle S^2 \rangle$[e]	R C–C/Å	R C–H/Å	<CCH/deg
1	HF/6-31G*[b]	−78.850 54	—	1.976	1.076	98.4
2	MP2 = FC/6-31G*[b]	−79.076 11	—	1.920	1.087	98.6
3	MP2 = Full/6-31G*	−79.084 79	0.758	1.918 8	1.086 7	98.60
4	MCSCF(3,8)/6-31G*[c]	−78.852 98	—	1.972 6	1.075 9	98.56
5	MCSCF(5,7)/6-31G*[c]	−78.874 46	—	1.963 9	1.077 8	98.10
6	HF/6-311G**	−78.875 84	0.759	1.961 2	1.077 0	98.42
7	MP2 = Full/6-31G**[d]	−79.130 73	—	1.918	1.082	98.3
8	CID = FC/6-311G**	−79.160 02	0.759	1.918 3	1.085 1	98.43
9	CISD = FC/6-311G**	−79.161 40	0.759	1.917 2	1.085 4	98.42
10	MP2 = Full/6-311G**	−79.181 56	0.760	1.906 5	1.087 2	98.38
11	CCD = FC/6-311G**	−79.183 89	0.759	1.919 1	1.089 4	98.37
12	QCISD = FC/6-311G**	−79.186 04	0.759	1.918 5	1.090 0	98.34
13	MP4 = FC/6-311G**	−79.191 06	0.760	1.914 9	1.090 7	98.33
14	ST4CCD = FC/6-311G**	−79.193 11	0.760	1.915 6	1.091 3	98.34
15	QCISD(T) = FC/6-311G**	−79.193 50	0.760	1.915 4	1.091 5	98.31

(b) ^2A_g (C_{2h})$_{DB}$ Entry	Optimization Level	Electronic energy (Hartree/particle)	$\langle S^2 \rangle$[e]	R C–C/Å	R C–H/Å	R C–H_2/Å	<CCH/deg	<CCH_2/deg
16	HF/6-311G**	Does not exist						
17	MP2 = Full/6-31G*	−79.084 77	0.760	1.549 6	1.148 3	1.087 4	85.11	116.16
18	MP2 = Full/6-31G**[c]	−79.131 29	—	1.579	1.131	1.081	82.6	115.8
19	MP2 = Full/6-311G**	−79.184 07	0.762	1.577 2	1.141 0	1.086 4	82.20	115.44
20	CID = FC/6-311G**	Does not exist						
21	CISD = FC/6-311G**	Does not exist						
22	CCD = FC/6-311G**	Does not exist						
23	QCISD = FC/6-311G**	−79.185 35	0.765	1.735 8	1.112 3	1.087 8	82.77	110.14
24	MP4 = FC/6-311G**	−79.191 50	0.763	1.645 9	1.130 0	1.088 9	81.46	113.45
25	ST4CCD = FC/6-311G**	−79.193 11	0.764	1.663 0	1.127 1	1.089 3	81.51	112.86
26	QCISD(T) = FC/6-311G**	−79.194 14	0.764	1.673 7	1.124 8	1.089 4	81.70	112.53

[a] The designations (c) and (b) alongside the structures follow Fig. 2. [b] From reference 1. [c] The MCSCF calculations in entry 4 involve three electrons in eight active orbitals. The MCSCF calculations in entry 5 involve five electrons in seven active orbitals. The orbital windows refer to the a_{1g} manifold. [d] From reference 3. [e] $\langle S^2 \rangle$ before annihilation of unwanted spin states. After annihilation, $\langle S^2 \rangle$ is always 0.750.

Table 3 Calculated relative energies[a] for the ^2A_g (C_{2h})$_{DB}$, $^2A_{1g}$ (D_{3d}), $^2A''$ (C_s) and ^2B_g (C_{2h}) structures of $C_2H_6^{+\bullet}$

				Relative energies[c]		
Entry	Computational level	Optimization level	^2A_g (C_{2h})$_{DB}$	$^2A_{1g}$ (D_{3d})	$^2A''$ (C_s)	^2B_g (C_{2h})
1	MP4	I	0.00	0.06 (0.33)	—(5.62)	—(5.92)
2	ST4CCD	I	0.00	−0.35 (−0.31)	—	—
3	QCISD(T)	I	0.00	0.09 (0.23)	—(5.14)	—(6.32)
4	MP2 = Full/6-31G*	II	0.00	−0.02	—	—
5	MP2 = Full/6-31G**[d]	II	0.00	0.35	—	—
6	MP2 = Full/6-311G**	II	0.00	1.57	4.82	4.13
7	MP4/6-311G**	II	0.00	0.28	—	—
8	ST4CCD/6-311G**	II	0.00	0.00	—	—
9	QCISD(T)/6-311G**	II	0.00	0.40	—	—

[a] In kcal mol^{-1}; 1 kcal mol = 4.184 kJ mol^{-1}. [b] Level I corresponds to the MP2 = Full/6-311G** optimized geometries. Level II involves internal optimization, *i.e.*, the energy and structure optimization are at the same specified level. [c] In parentheses are values obtained with an all-electron window. The other results refer to a frozen core window. [d] From reference 3.

Table 4 Vertical and adiabatic ionization potentials for C_2H_6

		E_i(v)/eV		E_i(a)/eV		E_i(a) (ΔH°)/eV[b]	
Entry	Method[a]	$^2A_{1g}$	^2E_g	$^2A_{1g}$	(^2A_g)$_{DB}$	$^2A_{1g}$	(^2A_g)$_{DB}$
1	HF/6-31G*	12.01	12.41	10.29	—	—	—
2	HF/6-311G**	11.95	12.31	10.23	—	10.11	—
3	MP2 = Full/6-311G**	13.06	12.58	11.62	11.55	11.48	11.39
4	MP4/6-311G**	12.63	12.61	11.53	11.51	11.41	11.38
5	ST4CCD/6-311G**	12.92	12.64	11.51	11.51	11.38	11.38
6	QCISD(T)/6-311G**	12.91	12.61	11.50	11.48	11.37	11.35

[a] These are all internally consistent levels (energies and geometries refer to the same levels). [b] Adiabatic E_i with thermal energy corrections for conversion to ΔH° scale. The corrections themselves are calculated from the MP2 = Full/6-311G** frequencies, moments of inertia, *etc.* The corrections are − 0.12 eV and −0.13 eV for the two isomers.

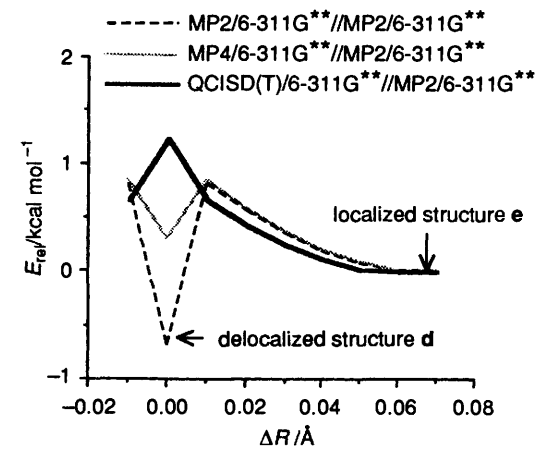

Fig. 3 MP4 = Full/6-311G**//MP2 = Full/6-311G** and QCISD-(T) = Full/6-311G**//MP2 = Full/6-311G** relative energies of the $^2A''$ (C_s) and ^2B_g (C_{2h}) isomers of $C_2H_6^{+\bullet}$ along the coordinate ΔR. The letters designating the two structures refer to Fig. 2.

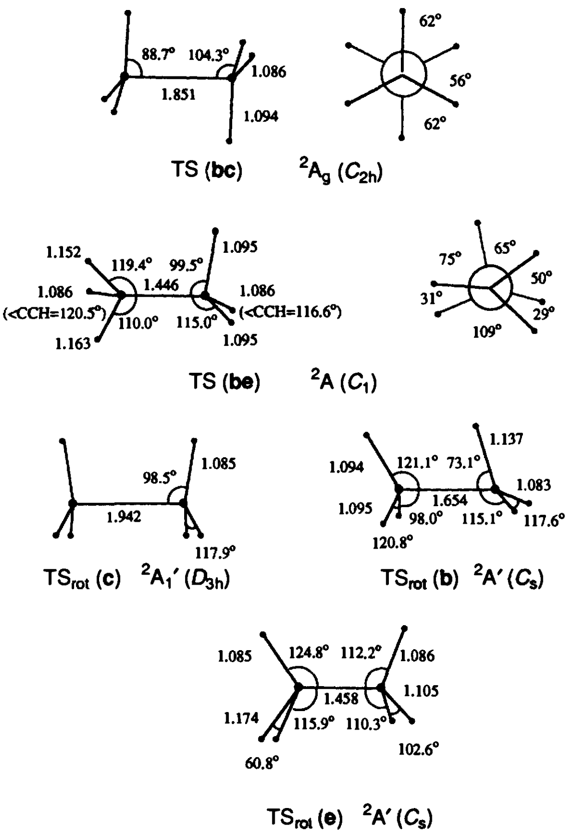

Fig. 4 Interconversion and internal rotation transition states, of the $C_2H_6^{+\bullet}$ isomers, located at the MP2 = Full/6-311G**//MP2 = Full/6-311G** level. An interconversion transition state (TS) is designated with a parenthetical pair of letters that specify the interconverting isomers. The internal rotation transition structure of a given isomer, specified by a letter, is designated as TS$_{rot}$.

now to report the vertical and adiabatic ionization potentials of C_2H_6, at the low-energy part of the PE spectrum. Table 4 shows the computed E_i data at various levels. It is seen that the ^2E_g identity of the first vertical E_i is established except for the Hartree–Fock levels which assign the first E_i(v) to $^2A_{1g}$. The individual vertical values themselves converge to 12.9 eV ($^2A_{1g}$) and 12.6 eV (^2E_g). The adiabatic potentials also converge quite fast to a value of *ca.* 11.5–11.6 eV which, upon inclusion of thermal correction, is further reduced to *ca.* 11.4 eV. While the computed adiabatic ionization potentials are in good agreement with the experimental *onset* of the PE spectrum,[5a] the closeness of the two electronic states and the softness of the surfaces should clearly complicate the spectrum by strong non-adiabatic effects,[24] so that straightforward assignment of the band maxima to the computed E_i(v) values is hardly possible in this case.

Interconversion Barriers and Transition States Between the $C_2H_6^{+\bullet}$ Isomers.—Fig. 4 shows the rotational and interconversion transition states which were located at the MP2 = Full/6-311G**//MP2 = Full/6-311G** level of optimization. Pseudo-rotational pathways which lead to scrambling of the bridging positions in the diboranoid structure were also considered, but no corresponding transition structure could be found even after an extensive search.

The first transition state in Fig. 4, TS (**bc**) possesses a C_{2h} point group symmetry and interconverts the two most stable isomers, $^2A_{1g}$ (D_{3d}) and ^2A_g (C_{2h})$_{DB}$. The second transition state, TS (**be**) possesses C_1 point-group symmetry and interconverts the diboranoid ^2A_g (C_{2h})$_{DB}$ and the localized $^2A''$ (C_s) structures. No connecting transition state was found between $^2A_{1g}$ (D_{3d}) and $^2A''$ (C_s), and any attempt to find transition states which may connect the ^2B_g (C_{2h}) structure to the others failed. This latter result is perhaps an indirect indication that the ^2B_g (C_{2h}) minimum may well be an artifact, as suggested by the QCISD(T) energy profile in Fig. 3. The remaining transition states, designated as TS$_{rot}$, correspond to the internal rotation modes of the three isomers.

The corresponding data for all the isomers and transition states are summarized in Table 5. Also included in Table 5 are thermochemical and entropic contributions which show that the interconversion barriers survive at the free energy and enthalpy levels. It is seen that all the structures possess internal rotation barriers which are larger than the interconversion barriers. This will, of course, affect the dynamics of these species at temperatures where these barriers are rate-limiting.

Discussion

Origins of the Electron-Shift Isomers and their Separating Barriers.—Owing to the complexity and subtlety of the computational results, it is helpful to establish a fundamental qualitative understanding of the nature of these $C_2H_6^{+\bullet}$ isomers and the factors which govern their interconversion barriers.

Referring back to the vertical configurations in Fig. 1, it is possible to predict the modes of stabilization available to the vertical states using two concepts of different complexity. At the orbital level, the nodal characteristics of the singly occupied MO in each configuration delineate the modes by which the vertical D_{3d} structures can relax and enjoy thereby an initial stabilization. This analysis was used in the classical review of Radom *et al.*[1] and will not be repeated here. The resulting structures are **c**, **d** and **f** which are, in turn, depicted in Fig. 2. We recall however, that, of them, only the $^2A_{1g}$ (D_{3d}) structure (**c**) is a true minimum while the ^2A_g (C_{2h}) and ^2B_g (C_{2h}) species (**f**, **d**) undergo further structural relaxations, the nature of which is governed by configuration mixing.[9,10] Since the configurations differ from each other by single electron shifts amongst the frontier orbitals in Fig. 1, following the rules of configuration mixings[10f] *the stabilization energies will be proportional to the overlap between those orbitals that participate in the electron shift as one moves from one configuration to the other.*

The key structure in the configuration mixing is in fact the wide-angled ^2A_g (C_{2h}) species (**f**, in Fig. 2) which acts as a pivot that generates the final structures by configuration mixing and avoiding crossings with the other two structures, as discussed below.

The $^2A_{1g}$ (D_{3d}) ⟶ ^2A_g (C_{2h}) Pathway.—Fig. 5(*a*) shows a

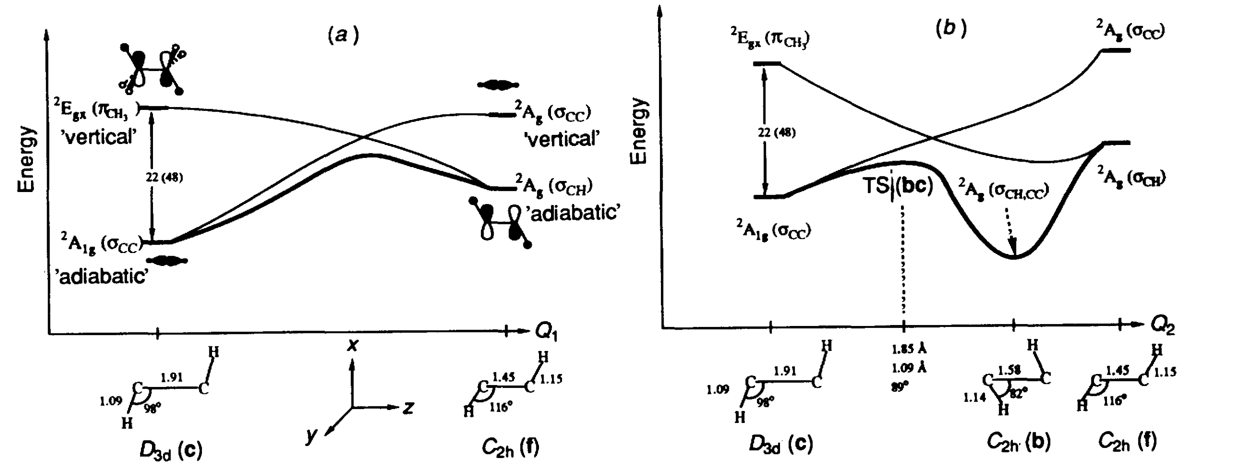

Fig. 5 Curve-crossing diagram showing (*a*) the interconversion of structures **c** and **f** along Q_1, and (*b*) the formation of **b** in the bridging pathway described by the coordinate Q_2 which involves in-plane HCC-angle narrowing. The orbitals in the drawings are the singly occupied MOs in the respective configurations. The heavy lines indicate adiabatic profiles after avoided crossing and configuration mixing. The diagram's gaps (in kcal mol^{-1}) on the left-hand side are computed at the MP2 = Full/6-311G** (HF/6-311G**) levels.

Shaik–Pross[10] avoided crossing diagram which interconverts the $^2A_{1g}$ (D_{3d}) and ^2A_g (C_{2h}) structures along a distortion coordinate, Q_1. The two end structures are shown on the Q_1 axis and correspond to the geometries of the structures **c** and **f**. The orbitals drawn alongside the curves are those which are singly occupied in the respective configurations, and the principal characters of these orbitals is indicated in the parentheses alongside the electronic state's Term-symbols. In addition, the ground configurations, being at their equilibrium geometries, are designated as 'adiabatic' while the excited states are designated as 'vertical', meaning the same geometry as the ground state but a different electronic structure.

At the D_{3d} point group, with a C–C distance of 1.91 Å, the $^2A_{1g}$ is the ground configuration possessing the odd electron in the σ_{CC} orbital, while the vertically excited state is the $^2E_{gx}$ component, in this case possessing the odd electron in the π_{CH_3}-type MO. As we move along the distortion coordinate by C–C bond shortening and in-plane C–H bond lengthening, the two configurations interchange their order, at the C_{2h} point-group extreme. Here with a C–C distance of 1.45 Å and in-plane C–H distances of 1.15 Å, the lowest configuration is the ^2A_g (C_{2h}) species which possesses the odd electron in a σ_{CH}-type orbital which is the distorted form of the π_{CH_3} orbital. At the same extreme, the vertical excited state is the one in which the odd electron is accommodated in the σ_{CC} orbital.

Except for the D_{3d} point-group, everywhere else the two configurations possess the same electronic symmetry, and therefore they can interact and avoid the crossing. The adiabatic energy profile after avoided crossing is indicated by the heavy line connecting the two ground-state structures *via* a barrier. According to the configuration mixing rule,[10f] the avoided crossing interaction and configuration mixing are proportional to the overlap of the two orbitals σ_{CC} and σ_{CH} which participate in the single electron shift between the configurations. The stabilization energy E_s due to configuration mixing is given by eqn. (1) using a perturbation theoretic expression, where the ΔE

$$E_s \propto |\langle\sigma_{CC}\,|\,\sigma_{CH}\rangle|^2/\Delta E \qquad (1)$$

is the configuration energy gap.

Even though the two orbitals possess the same symmetry under C_{2h}, they overlap quite poorly because the wide in-plane HCC angle prohibits a good overlap between the hydrogens and the lobes of the σ_{CC} orbital. A good overlap of the two orbitals will occur if the two in-plane hydrogens will move to bridging positions, with the HCC angle smaller than 90°. This *maximum overlap requirement* is the major reason why the ground ^2A_g (C_{2h}) structure (**f**) does not survive as a true minimum and undergoes further distortion to the diboranoid structure.

The avoided crossing along the bridging pathway to the diboranoid structure is depicted in Fig. 5(*b*). Thus, by allowing the in-plane hydrogens to bridge along the Q_2 coordinate, the $\langle\sigma_{CC}\,|\,\sigma_{CH}\rangle$ overlap increases considerably. The configuration mixing thereby becomes significantly stabilizing and generates therefore the diboranoid minimum, $^2A_g(C_{2h})_{DB}$, which is derived from the wide-angled ^2A_g (C_{2h}) structure but now possesses an odd electron in an orbital of mixed σ_{CC}–σ_{CH} character. Similarly, the avoided crossing generates the transition state for the interconversion of the $^2A_{1g}$ (D_{3d}) and ^2A_g $(C_{2h})_{DB}$ electron-shift isomers.

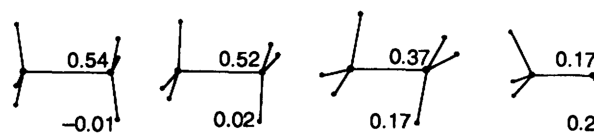

c TS (**bc**) **b** **f**

1 **2** **3** **4**

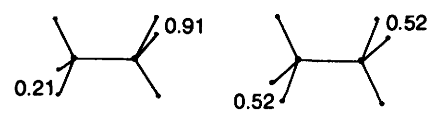

e **d**

5 **6**

The computed spin density distribution on the *in-plane* hydrogens in the four structures of Fig. 5(*b*) is shown in **1**–**4** and further illustrates the electronic relationships between the structures. It is seen that in the $^2A_{1g}$ (D_{3d}) structure, **1**, the in-plane spin density is negative while in the wide-angled ^2A_g (C_{2h}) structure, **4**, these spin densities are substantially positive. The spin density of the diboranoid structure, **3**, is seen to be very close to that in **4**, thus corroborating the proposed wide-angled—^2A_g (C_{2h})—derivation of the diboranoid isomer. The transition state (TS), **2**, acquires some very small positive spin density which again indicates that the TS lies closer to the $^2A_{1g}$ (D_{3d}) isomer, as depicted in Fig. 5(*b*).

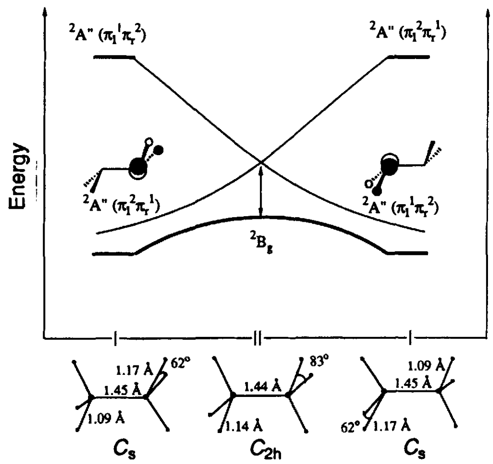

Fig. 6 Curve-crossing diagram showing the interconversion of the mixed-valent $^2A''$ (C_s) structures through the monovalent ^2B_g (C_{2h}) transition structure which is obtained by avoiding crossing (heavy line). The electronic configurations in the two localized orbitals CH_2 orbitals, π_l (l = left) and π_r (r = right), are indicated in parentheses.

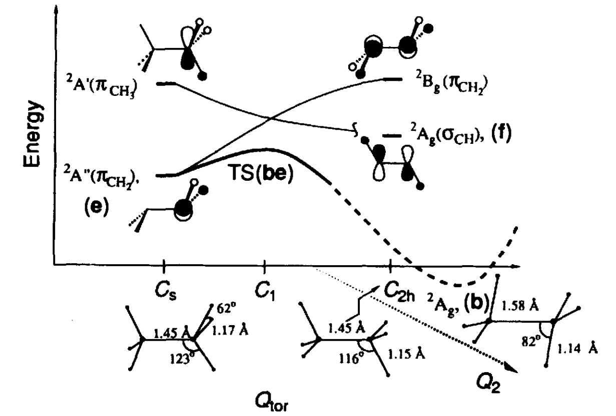

Fig. 7 Curve-crossing diagram showing the interconversion of the localized (**e**) and diboranoid (**b**) isomers along a pathway which involves two phases. The regular line is the torsional phase (Q_{tor}) which involves a transformation from C_s to C_{2h} *via* C_1, and the dashed line is a bridging phase (Q_2) which involves in-plane HCC-angle narrowing. The adiabatic curve is drawn with different line-types as it changes course from Q_{tor} to Q_2.

The definition 'electron-shift isomerism' now becomes more evident in the light of the above spin-density analysis and of the orbital-to-orbital electron shift which accompanies the curve crossing in Fig. 5. Thus, it is apparent that *the* $^2A_{1g}$ (D_{3d}) *and* ^2A_g $(C_{2h})_{DB}$ *isomers conserve the structural connectivity of the neutral parent molecule, albeit with modified geometric details, and are mutually related by a shift of an electron from the* C–C *fragment to the in-plane* H–C *fragments.*

This is an appropriate point at which to address the computational behaviour of the diboranoid isomer which exists only at the correlated levels but not at the Hartree–Fock levels, even with a triple zeta basis set such as 6-311G** which also includes polarization functions on the hydrogens. The computed diagram's energy gap, in Fig. 5, which is 22 kcal mol^{-1} at the MP2 level and 48 kcal mol^{-1} at the Hartree-Fock level,* provides a clue to these findings. The larger gap at the Hartree–Fock level is obtained because this level underestimates the stability of the ^2E_g configuration (see Table 4). As may be seen from Fig. 5, the higher the ^2E_g configuration the less stable will be the initial adiabatic structure, **f**, thereby exerting similar instability on the diboranoid structure which is derived from **f**. Thus, the same computational factors which overestimate the $E_i(v)$ value for ionization to the ^2E_g state are the very factors which preclude the existence of the diboranoid structure. Following this analysis we may conclude that the correlated levels which reproduce well the vertical ionization potentials also provide the definitive result that the diboranoid isomer is a true minimum. This analysis highlights the utility of the curve crossing model for analysis of complex computational results.

The $^2A''$ (C_s) $\longrightarrow$ ^2B_g (C_{2h}) *Pathway*.—The interconversion of the mirror image $^2A''$ (C_s) isomers through a ^2B_g (C_{2h}) transition state can be understood by inspecting the computed CH_2 group spin densities for the $^2A''$ (C_s) and ^2B_g (C_{2h}) structures in **5** and **6**. It is seen that in the $^2A''$ isomer, **5**, the odd-electron is largely located (*ca.* 0.91 spin) on the CH_2 group which possesses longer C–H bonds and a smaller H–C–H angle (the other H atoms possess negative spin densities). On the other hand, the ^2B_g (C_{2h}) structure, **6**, delocalizes the spin equally over the two CH_2 moieties. The relationship between the two structures is precisely that which exists between mixed-valent (localized) and mono-valent (delocalized) structures, in organometallic complexes and can be represented by the Marcus–Hush model[25] of intramolecular electron transfer. From previous experience with mixed- and mono-valent situations[23] the two structural types do not coexist unless a third electronic configuration interferes and mixes preferentially with one of the types. Thus, in most cases a stable mixed-valent structure requires a mono-valent transition structure and *vice versa*. In the present case, the QCISD(T) results (Fig. 3) appear to corroborate the general conclusion that the two bonding situations are mutually exclusive.

Fig. 6, which is constructed following the QCISD(T) results (Fig. 3), illustrates the formation of the energy profile for the interconversion of mirror-image mixed-valent structures using a Marcus–Hush curve crossing diagram. Much the same as in Fig. 5, here too are shown the singly occupied orbitals which are the right-hand- and left-hand-side π_{CH_2}-type orbitals (π_r and π_l). Along the C_s–C_{2h}–C_s distortion coordinate the two localized structures interconvert, and by avoided crossing generate the transition structure which is the delocalized ^2B_g (C_{2h}) species. *Thus, the two* $^2A''$ (C_s) *structures behave as two mirror-image electron-shift isomers which shift the electron between the right and left* CH_2 *fragments.*

How definitive is the QCISD(T) results which favour the mixed-valent situation? This question is subtle because, in terms of Fig. 6, the final result is obtained as a delicate balance between the height of the crossing point and the difference in configuration mixing near the localized geometries in comparison with the crossing point.[23] An approximate estimate of 25 kcal mol^{-1} for the diagram's gap may be obtained from the computational results.† Using a model of two intersecting parabolae for the two diabatic curves[25] in Fig. 6 leads to a crossing point which is *ca.* 6 kcal mol^{-1} higher than the diabatic localized structures. This in turn means that, in order to find a ^2B_g (C_{2h}) ground state, the configuration mixing at the crossing point will have to be > 6 kcal mol^{-1} larger than the same mixing in the C_s geometries for the localized structures, Considering that the configuration mixing is dominated by the C–C

* The gaps for the 6-31G* basis set are correspondingly 49 kcal mol^{-1} (UHF) and 23 kcal mol^{-1} (UMP2) and for the 6-31G basis set they are 50 kcal mol^{-1} (UHF) and 30 kcal mol^{-1} (UMP2), respectively.

† The diagram's energy gap in Fig. 6 is the sum of relaxation energies for the two CH_2 moieties. It was not possible to calculate this gap by guess alteration owing to variational collapse. An estimate for that is the relaxation energy of the vertical ^2E_g configuration, which at the QCISD(T) level amounts to 1.13 eV.

Table 5 Energy and thermochemistry of the $C_2H_6^{+\bullet}$ isomers[a] and the various transition states (TS)

Structure	Electronic energy[d]	E_{zp} (Hartree/particle)	E_{th} (Hartree/particle)	S/cal mol^{-1} K^{-1} [f]	E_{rel}/kcal mol^{-1} MP2[g]	MP2 + E_{zp}	$\Delta\Delta H°$	$\Delta\Delta G$
b	−79.184 07	0.069 62	0.073 47	60.457	0.00 (0.00)	0.00	0.00	0.00
TS_{rot} (**b**)[b]	−79.177 78	0.068 69	0.072 41	60.212	3.95	3.37	3.29	3.36
TS (**bc**)[c]	−79.181 25	0.069 52	0.073 42	59.830	1.77	1.71	1.74	1.93
TS (**be**)[c]	−79.175 68	0.065 17	0.068 93	60.117	5.27	2.48	2.42	2.52
c	−79.181 56	0.069 82	0.074 34	63.353	1.58 (0.40)	1.71	2.13	1.27
TS_{rot} (**c**)[b]	−79.178 33	0.068 79	0.073 22	63.687	2.02	3.08	3.45	2.49
d	−79.177 49	0.070 98	0.074 82	60.298	4.13 (6.32)	4.98	4.98	5.03
e	−79.176 39	0.067 38	0.071 38	61.288	4.82 (5.14)	3.42	3.51	3.26
TS_{rot} (**e**)[b]	−79.174 35	0.067 09	0.070 50	58.859	6.10	4.24	4.52	5.00

[a] The isomer descriptors refer to Fig. 2. [b] These are the transition states for internal rotation of the species indicated in parentheses. [c] These are the transition states for interconversion of the species indicated in parentheses. [d] Electronic energies in Hartree/particle (H/p) at the MP2 = Full/6-311G**//MP2 = Full/6-311G** level. [e] Total thermal energy contribution to the electronic energy. [f] Refers to a standard state of 1 atm and 298.15 K. [g] In parentheses are QCISD(T) energies.

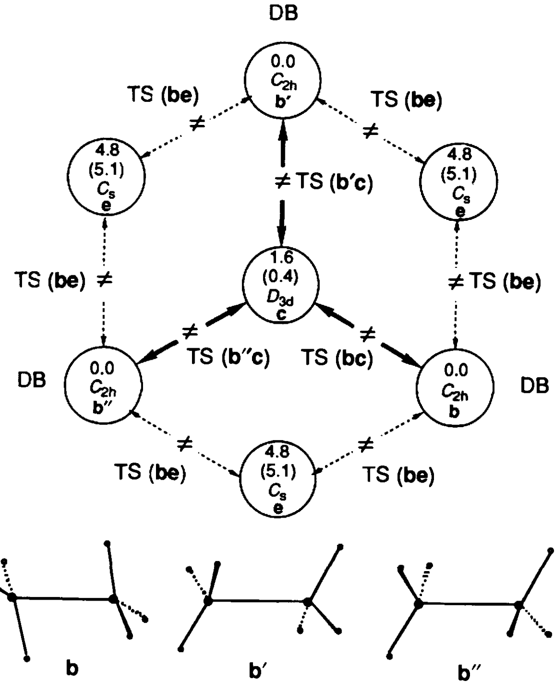

Fig. 8 A proposed scrambling mechanism of the bridging positions in the diboranoid structure (DB). There are two possible scrambling pathways: (*i*) the pathways drawn by heavy arrows proceeds from ^2A_g $(C_{2h})_{DB}$ to $^2A_{1g}$ (D_{3d}), and (*ii*) the pathways with the dashed lines connect ^2A_g $(C_{2h})_{DB}$ to $^2A''$ (C_s). The first mechanism, indicated by the heavy arrows, is the low-energy pathway which also avoids the traditional Jahn–Teller mechanism. The three diboranoid structures corresponding to **b**, **b′** and **b″** are shown below the hexagon. The relative energies of the various species (in kcal mol^{-1}) are indicated near them and correspond to the MP2 = Full/6-311G**//MP2 = Full/6-311G** results, and, in parentheses, to the QCISD(T)/6-311G**//MP2 = Full/6-311G** results.

distance, which determines the π-type overlap of the 2p(C) AOs of the fragment orbitals in Fig. 6, and that this distance is quite close for the two structures, it is likely that the configuration mixing difference does not exceed 6 kcal mol^{-1}. We are led to conclude therefore that the QCISD(T) result is probably correct, and that the mixed-valent $^2A''$ (C_s) isomers are likely to be the real minima, with ^2B_g (C_{2h}) being the transition structure.

The $^2A''$ $(C_s) \longrightarrow {^2A_g}$ $(C_{2h})_{DB}$ Pathway.—To understand this pathway it is more instructive to consider the avoided crossing in two distinct phases, as described in Fig. 7. The first phase involves the avoided crossing of the $^2A''$ (C_s) isomer with the wide-angled ^2A_g (C_{2h}) species, and the second phase involves the configuration mixing owing to the bridging deformation which generates the diboranoid structure, as already discussed for Fig. 5. At the C_s point-group symmetry, the ground structure is the $^2A''$ state, possessing the odd electron in the π_{CH_2} orbital which is drawn near the electronic Term-symbol. The vertical excited state is $^2A'$ in which the odd electron resides in the π_{CH_3} orbital (also drawn near the corresponding state). At the C_{2h} point-group symmetry, still in the first phase, these states interconvert and become the ^2A_g and ^2B_g pair. Since the electron shift takes place between the two mutually perpendicular orbitals, the mixing of the two configurations will also depend on the overlap of these orbitals. The only way to mix the mutually perpendicular orbitals is if the reaction coordinate loses all symmetry (becomes C_1) and involves a torsion which will allow the two sets of hydrogens to overlap with the two p-type AOs of the carbon atom. This means that we expect a C_1-type transition state which involves a dominant torsional mode along with some changes of C–H bond lengths and H–C–H angles, as is indeed borne out by the computational results.

Past the transition state, there begins the second phase where the in-plane hydrogens move to bridging positions and the transformation coordinate changes course accordingly as indicated in the figure by Q_2. Along this coordinate the wide-angled ^2A_g (C_{2h}) structure (**f**), which is not a true minimum, rolls down with no barrier to the diboranoid isomer ^2A_g $(C_{2h})_{DB}$ owing to the configuration mixing described above in Fig. 5(*b*). In this manner, the C_1 transition state connects the $^2A''$ (C_s) and ^2A_g $(C_{2h})_{DB}$ isomers by shifting an electron between the two mutually perpendicular orbitals, derived from the $1e_g$ set in the vertical state.

The Relationship between the Computational Results and the Low- and High-temperature EPR Data.—The most stable isomer is the diboranoid, ^2A_g $(C_{2h})_{DB}$ which is surrounded by barriers in the range *ca.* 1–5 kcal mol^{-1} (Table 5). At a temperature as low as 4.2 K, these barriers are sufficient virtually to freeze the diboranoid isomers as the only existing EPR-active species. The spin-density distribution (in **3**) would predict a 1:2:1 line pattern, and, as was shown by Lunel and Huang,[3] the computed hyperfine coupling constants match very well the experimental results.

At higher temperatures, > 77 K, some of the barriers may become sufficiently small to allow scrambling of the hydrogens in the diboranoid structure. In agreement with the conclusion of Iwasaki and collaborators,[8] our computational results show that the internal rotational process should be sluggish owing to the significant barrier of *ca.* 4 kcal mol^{-1} (Table 5). Also, since all our attempts to elucidate a low-energy pseudo-rotation scrambling mechanism for a diboranoid failed we are led to conclude that the scrambling mechanism is likely to occur *via* the isomerization pathways.

Fig. 8 depicts the possible pathways which connect the diboranoid isomer ^2A_g $(C_{2h})_{DB}$ to the other two electron-shift isomers, and shows that the fastest process is the interconversion of ^2A_g $(C_{2h})_{DB}$ to the $^2A_{1g}$ (D_{3d}). Each event of $^2A_{1g}$ (D_{3d}) formation will, in turn, be followed by a faster reverse process, back to ^2A_g $(C_{2h})_{DB}$, which will be formed in three equivalent forms, **b**, **b′**, and **b″** which differ in the identity of the pair of hydrogens in the bridging positions. Since the equilibrium constant at 77 K is expected to be rather small, the EPR spectrum will still be dominated by the emission of the three unique diboranoid structures, and will therefore exhibit the characteristic large hyperfine coupling constant. However, the high-temperature value of the coupling constant will be a third of the original low-temperature value owing to the fast scrambling of the bridging hydrogens which determine the coupling constants.

The scrambling mechanism in Fig. 8 appears, at first sight similar, to be the traditional picture of Jahn–Teller dynamics, but actually there exists a fundamental difference. In the traditional Jahn–Teller pathway the actual dynamics skips the original molecular symmetry to avoid the degenerate high-energy state. The movement occurs along the rim of the 'Mexican-hat', passing through the structures which are derived from the Jahn–Teller distortions. In the present case, the expected Jahn–Teller mechanism is the ^2A_g $(C_{2h})_{DB} \longrightarrow {}^2A''$ (C_s) pathway along the dashed edges of the hexagon in Fig. 8. However, since the $^2A''$ (C_s) structures are high-lying, this mechanism is inactive and is replaced by the ^2A_g $(C_{2h})_{DB} \longrightarrow {}^2A_{1g}$ (D_{3d}) mechanism that proceeds through the original D_{3d} symmetry. Thus, the $3a_{1g}$–$1e_g$ orbital proximity in C_2H_6 provides a low-energy mechanism which passes through the adiabatic $^2A_{1g}$ structure in the original symmetry, thereby avoiding the traditional Jahn-Teller dynamics. Our story, then, ends where it begins, that the $3a_{1g}$–$1e_g$ orbital proximity in ethane endows its cation radicals with most of its unusual characteristics.

Conclusions

The present computational study of the $C_2H_6^{+\bullet}$ surface establishes, at the QCISD(T)/6-311G** level of theory, that $C_2H_6^{+\bullet}$ possesses three ground-state isomers. The most stable isomer is ^2A_g $(C_{2h})_{DB}$, which is derived from the Jahn–Teller-active ^2E_g (D_{3d}) state by a distortion which reduces the point-group symmetry to C_{2h}, and has two bridging hydrogens in a diboranoid structure. The least stable isomer (by *ca.* 4.8–5.1 kcal mol^{-1}) is $^2A''$ (C_s) which arises from a ^2B_g (C_{2h}) structure by a localizing distortion. This distortion pins down the odd electron in one of the CH_2 groups, in comparison with the electron delocalization which is present in the ^2B_g (C_{2h}) structure. The latter structure is also derived from the same ^2E_g (D_{3d}) state by a symmetry-breaking distortion. The second most stable isomer (*ca.* 0.4–1.6 kcal mol^{-1} above the diboranoid structure) is the $^2A_{1g}$ (D_{3d}) structure which preserves the original point-group symmetry of ethane.

Two interconversion pathways are found to link the diboranoid ^2A_g $(C_{2h})_{DB}$ isomer to the other two isomers. The lowest-energy mechanism appears to be the one linking ^2A_g $(C_{2h})_{DB}$ and $^2A_{1g}$ (D_{3d}). Each event of $^2A_{1g}$ (D_{3d}) formation is, in turn, followed by a faster reverse process which scrambles the bridging hydrogens. *Thus, we have identified a low-energy mechanism which funnels the dynamics through the original point-group symmetry, away from the traditional Jahn–Teller dynamics through the* $C_{2h} \longrightarrow C_s$ *pathway*. These results form the basis of an interpretation of the observed EPR spectrum (reference 8) in the low- and high-temperature studies. Thus, the low-temperature (4.2 K) EPR signals are emitted by a single ^2A_g $(C_{2h})_{DB}$ species with two unique bridging hydrogens which possess high spin-densities and thereby account for the observed large hyperfine splitting constant of 150 G (reference 3). On the other hand, at the high-temperature limit (77 K) the EPR signals are emitted from three unique ^2A_g $(C_{2h})_{DB}$ diboranoid species which undergo fast scrambling of their bridging positions, thereby reducing, by a factor of three, the observed hyperfine coupling constants.

A qualitative analysis[9,10] of the origins of the various isomers and their interconversion pathways shows that a useful way to understand the results is in terms of '*electron-shift isomerism*' in which single electron-shifts among different fragments of the atomic skeleton generate both the $C_2H_6^{+\bullet}$ isomers as well as their intervening transition structures.

Acknowledgements

This research is supported in part by a grant (to S.S.) from the Basic Research Foundation Administered by the Israel Academy of Sciences and Humanities. The authors are grateful to the Ministry of Absorption, the Wolfson Foundation and the Ministry of Science and Technology for supporting A. I. The authors are indebted to L. Radom for his witty proposal, which enable us to solve the dichotomy between 'localized' and 'delocalized' structures of $C_2H_6^{+\bullet}$. S. S. is obliged to J. P. Dinnocenzo for an exciting discussion leading to the definition of 'electron-shift' isomerism.

References

1 W. J. Bouma, D. Poppinger and L. Radom, *Isr. J. Chem.*, 1983, **23**, 21.
2 D. J. Belville and N. L. Bauld, *J. Am. Chem. Soc.*, 1982, **104**, 5700.
3 S. Lunel and M.-B. Huang, *J. Chem. Soc., Chem. Commun.*, 1989, 1031.
4 (*a*) J. W. Rabalais and A. Katrib, *Mol. Phys.*, 1974, **27**, 923; (*b*) K. Kimura, S. Katsumata, Y. Achiba, T. Yamazaki and S. Iwata, *Handbook of the He I Photoelectron Spectra of Fundamental Organic Molecules*, Japan Scientific Soc. Press, Tokyo, 1981; (*c*) S. Day, A. J. Dixon, I. E. McCarthy and E. Weigold, *J. Electron Spectrosc. Relat. Phenom.*, 1976, **7**, 397.
5 (*a*) E. Heilbronner, in *The Chemistry of Alkanes and Cycloalkanes*, eds. S. Patai and Z. Rappoport, Wiley, NY, 1992, chap. 10; (*b*) A. Reichartz, R. J. Buenker, P. J. Bruna and S. D. Peyerimhoff, *Mol. Phys.*, 1977, **33**, 1345; (*c*) A. Reichartz, R. J. Buenker and S. D. Peyerimhoff, *Chem. Phys.*, 1978, **28**, 305; R. J. Buenker and S. D. Peyerimhoff, *Chem. Phys.*, 1975, **8**, 56; (*d*) L. S. Cederbaum, W. Domcke, J. Schirmer, W. von Niessen, G. H. F. Diercksen and W. P. Craemer, *J. Chem. Phys.*, 1978, **69**, 1591; (*e*) W. A. Lathan, L. A. Curtis and J. A. Pople, *Mol. Phys.*, 1971, **22**, 1081.
6 T. Koopmans, *Physica*, 1939, **1**, 104.
7 C. Møller and M. S. Plesset, *Phys. Rev.*, 1934, **46**, 618.
8 (*a*) M. Iwasaki, K. Toriyama and K. Nunome, *J. Am. Chem. Soc.*, 1981, **103**, 3591; (*b*) K. Toriyama, K. Nunome and M. Iwasaki, *J. Phys. Chem.*, 1981, **85**, 2149; *J. Chem. Phys.*, 1982, **77**, 5891.
9 S. S. Shaik, *J. Am. Chem. Soc.*, 1981, **103**, 3692.
10 (*a*) S. Shaik, *Pure Appl. Chem.*, 1991, **63**, 195; (*b*) A. Pross and S. S. Shaik, *Acc. Chem. Res.*, 1983, **16**, 363; (*c*) S. S. Shaik, H. B. Schlegel and S. Wolfe, *Theoretical Aspects of Physical Organic Chemistry. Application to the* S_N2 *Transition State*, Wiley-Interscience; NY, 1992; (*d*) T. H. Lowry and K. S. Richardson, *Mechanism and Theory in Organic Chemistry*, Harper and Row; NY, 1987, pp. 604–608; 359–360; (*e*) S. S. Shaik and P. C. Hiberty, in *Theoretical Concepts for Chemical Bonding*, ed. Z. B. Maksic, Springer, Berlin, 1991; Vol. 4, p. 324; (*f*) S. S. Shaik, in *New Theoretical Concepts for Understanding Organic Reactions*, eds. J. Bertran and G. I. Csizmadia, NATO ASI Series C267, Kluwer, Dordrecht, The Netherlands, 1989, p. 165.
11 M. J. Frisch, M. Head-Gordon, G. W. Trucks, J. B. Foresman, H. B. Schlegel, K. Raghavachari, M. Robb, J. S. Binkley, C. Gonzalez, D. J. Defrees, D. J. Fox, R. A. Whiteside, R. Seeger, C. F. Melius, J. Baker, R. L. Martin, L. R. Kahn, J. J. P. Stewart, S. Topiol and J. A. Pople, GAUSSIAN 90, *Revision J*, Gaussian, Inc.; Pittsburgh PA, 1990.
12 M. J. Frisch, G. W. Trucks, M. Head-Gordon, P. M. W. Gill, M. W. Wong, J. B. Foresman, B. G. Johnson, H. B. Schlegel, M. A. Robb, E. S. Replogle, R. Gomperts, J. L. Andres, K. Raghavachari, J. S. Binkley, C. Gonzalez, R. L. Martin, D. J. Fox,

D. J. Defrees, J. Baker, J. J. P. Stewart and J. A. Pople, GAUSSIAN 92, *Revision B*, Gaussian, Inc., Pittsburgh PA, 1992.
13 W. J. Hehre, L. Radom, P. v. R. Schleyer and J. A. Pople, *Ab Initio Molecular Orbital Theory*; Wiley–Interscience, NY, 1986.
14 R. Krishnan, J. S. Binkley, R. Seeger and J. A. Pople, *J. Chem. Phys.*, 1980, **72**, 650.
15 R. Krishnan and J. A. Pople, *Int. J. Quantum Chem.*, 1978, **14**, 91; R. Krishnan, M. J. Frisch and J. A. Pople, *J. Chem. Phys.*, 1980, **72**, 4244.
16 J. A. Pople, R. Seeger and R. Krishnan, *Int. J. Quantum Chem. Symp.* 1977, **11**, 149.
17 J. A. Pople, R. Krishnan, H. B. Schlegel and J. S. Binkley, *Int. J. Quantum Chem.*, 1978, **14**, 545.
18 K. Raghavachari, *J. Chem. Phys.*, 1985, **82**, 4607.
19 J. A. Pople, M. Head-Gordon and K. Raghavachari, *J. Chem. Phys.*, 1987, **87**, 5968.
20 R. H. E. Eade and M. A. Robb, *Chem. Phys. Lett.*, 1981, **83**, 362; D. Hegarty and M. A. Robb, *Mol. Phys.*, 1979, **38**, 1795.
21 P. C. Hariharan and J. A. Pople, *Theor. Chim. Acta*, 1973, **38**, 213.
22 H. B. Schlegel, *J. Comput. Chem.*, 1982, **3**, 214.
23 (*a*) S. S. Shaik, P. C. Hiberty, G. Ohanessian and J. M. Lefour, *J. Phys. Chem.*, 1988, **92**, 5086; (*b*) S. S. Shaik and M. H. Whangbo, *Inorg. Chem.*, 1986, **26**, 1201.
24 H. Køppel, L. S. Cederbaum, W. Domcke and S. S. Shaik, *Angew. Chem., Int. Ed. Engl.*, '983, **22**, 210.
25 (*a*) R. A. Marcus, *Annu. Rev. Phys. Chem.*, 1964, **15**, 155; (*b*) N. S. Hush, *Prog. Inorg. Chem.*, 1967, **8**, 391.

Paper 3/01191G
Received 1*st March* 1993
Accepted 5*th April* 1993

Appendix

Tables A1–A3: compilation of structures and energies of $C_2H_6^{+\bullet}$ isomers.

Table A.1 Total electron energies of C_2H_6 and $C_2H_6^{+\bullet}$ isomers

		Total electron energy (Hartree/particle)				
		C_2H_6	$C_2H_6^{+\bullet}$-vertical		$C_2H_6^{+\bullet}$-adiabatic	
Post-SCF option[a]	Method[b]	$^1A_{1g}$	$^2A_{1g}$	^2E_g	$^2A_{1g}$ (D_{3d})	^2A_g (C_{2h})$_{DB}$
Basis set 6-31G*						
HF[c]	1	−79.228 75	−78.787 31	−78.772 86	−78.850 54	−78.816 31[d]
MP2[c]	1a	−79.494 74	−79.022 99	−79.039 70	−79.076 11	—
MP2	1b	−79.503 97	−79.031 60	−79.051 03	−79.084 79	−79.084 77
Basis set 6-311G**						
HF	1	−79.251 71	−78.812 43	−78.799 27	−78.875 84	−78.848 20[d]
MP2	1b	−79.608 59	−79.128 53	−79.146 41	−79.181 56	−79.184 07
MP2	2a	−79.570 89	−79.091 06	−79.108 74	−79.144 67	−79.146 67
MP3	2a	−79.601 21	−79.124 79	−79.136 55	−79.179 78	−79.178 00
MP3	2b	−79.640 49	−79.163 86	−79.175 77	−79.218 29	−79.217 00
MP4D	2a	−79.609 56	−79.133 27	−79.144 94	−79.188 20	−79.186 18
MP4D	2b	−79.648 92	−79.172 41	−79.184 24	−79.226 76	−79.225 24
MP4DQ	2a	−79.603 72	−79.128 35	−79.137 71	−79.183 35	−79.180 54
MP4DQ	2b	−79.642 84	−79.167 28	−79.176 76	−79.221 72	−79.219 38
MP4SDQ	2a	−79.605 40	−79.130 10	−79.139 94	−79.184 82	−79.182 61
MP4SDQ	2b	−79.644 62	−79.169 12	−79.179 09	−79.223 27	−79.221 55
MP4SDTQ	2a	−79.614 55	−79.136 90	−79.150 84	−79.191 00	−79.191 01
MP4SDTQ	2b	−79.654 03	−79.176 16	−79.190 27	−79.229 67	−79.230 20
MP4SDTQ	1a	−79.614 64	−79.150 40	−79.151 14	−79.191 06	−79.191 50
CID	2a	−79.573 82	−79.104 21	−79.110 01	−79.159 98	−79.155 29
CID	2b	−79.609 10	−79.139 55	−79.145 21	−79.194 82	−79.190 49
CID	1a	−79.573 83	−79.104 43	−79.109 50	−79.160 02	—
CISD	2a	−79.575 09	−79.105 85	−79.111 84	−79.161 37	−79.157 08
CISD	2b	−79.610 41	−79.141 18	−79.147 03	−79.196 21	−79.192 26
CISD	1a	−79.575 10	−79.106 12	−79.111 37	−79.161 40	—
CCD	2a	−79.604 21	−79.128 87	−79.137 72	−79.183 85	−79.180 84
CCD	2b	−79.643 28	−79.167 74	−79.176 73	−79.222 14	−79.219 63
CCD	1a	−79.604 24	−79.130 08	−79.137 13	−79.183 89	—
ST4CCD	2a	−79.615 79	−79.138 94	−79.151 74	−79.193 03	−79.192 47
ST4CCD	2b	−79.655 22	−79.178 15	−79.191 11	−79.231 65	−79.231 60
ST4CCD	1a	−79.615 98	−79.140 97	−79.151 43	−79.193 11	−79.193 11
QCISD	2a	−79.606 16	−79.131 50	−79.140 61	−79.186 00	−79.183 90
QCISD	2b	−79.645 34	−79.170 47	−79.179 71	−79.224 38	−79.222 80
QCISD	1a	−79.606 21	−79.132 84	−79.140 94	−79.186 04	−79.185 35
QCISD(T)	2a	−79.615 81	−79.139 52	−79.152 21	−79.193 43	−79.193 28
QCISD(T)	2b	−79.655 25	−79.178 74	−79.191 59	−79.232 05	−79.232 42
QCISD(T)	1a	−79.615 92	−79.141 52	−79.152 54	−79.193 50	−79.194 14

[a] For all calculations $\langle S^2 \rangle$ before annihilation of unwanted spin states did not exceed 0.770, after annihilation $\langle S^2 \rangle$ was always 0.750. [b] Methods: 1, 'internal' optimization (*e.g.* MP2/6-311G**//MP2/6-311G**); 2, single-point calculation at MP2/6-311G** optimized geometry, for all post-SCF options: a, frozen-core approximation; b, all-electron window. [c] From ref. 1. [d] $^2A''$ for C_s symmetry, see Table 1 and ref. 1.

Table A.2 Total adiabatic electron energies of other $C_2H_6^{+\bullet}$ isomers

Post-SCF option[a]	Method[b]	Total electron energy (Hartree/particle)				
		$^2A''$ (C_s)	^2B_g (C_{2h})	^2A_g (C_{2h})	^2A_u (C_{2h})	^2B_u (C_{2h})
Basis set 6-31G*						
HF[c]	1	−78.816 31	−78.807 58	—	—	—
MP2[c]	1a	−79.069 98	−79.064 61	—	—	—
MP2	1b	—	−79.079 56	—	−78.973 91	−78.973 22
Basis set 6-311G**						
HF	1	−78.848 20	−78.834 83	—	−78.718 64	−78.717 97
MP2	1b	−79.176 39	−79.177 49	−79.172 97	−79.072 85	−79.071 54
MP4SDTQ	2b	−79.221 24	−79.220 75	—	—	—
QCISD(T)	2b	−79.224 23	−79.222 35	—	—	—

[a–c] See corresponding footnotes to Table A.1.

Table A.3 Optimized geometry of C_2H_6 and isomers of $C_2H_6^{+\bullet}$

Optimization Level	R C–C/Å	R C–H/Å	<CCH/deg
C_2H_6, $^1A_{1g}$			
HF/6-31G* (ref. 1)	1.528	1.086	111.2
MP2 = FC/6-31G* (ref. 1)	1.526	1.093	111.2
HF/6-311G**	1.526 7	1.086 2	111.20
MP2 = Full/6-31G*	1.524 6	1.092 9	111.19
MP2 = Full/6-311G**	1.527 0	1.092 9	111.15
CID = FC/6-311G**	1.528 2	1.091 1	111.14
CID = Full/6-311G**	1.525 9	1.090 3	111.16
CISD = FC/6-311G**	1.528 5	1.091 4	111.14
CISD = Full/6-311G**	1.526 1	1.090 6	111.16
CCD = FC/6-311G**	1.532 3	1.095 4	111.12
CCD = Full/6-311G**	1.530 0	1.094 9	111.14
ST4CCD = FC/6-311G**	1.535 3	1.097 5	111.08
ST4CCD = Full/6-311G**	1.533 3	1.097 0	111.11
QCISD = FC/6-311G**	1.532 8	1.096 1	111.12
QCISD = Full/6-311G**	1.530 4	1.095 5	111.15
QCISD(T) = FC/6-311G**	1.535 1	1.097 4	111.08
QCISD(T) = Full/6-311G**	1.533 1	1.096 9	111.11
MP4 = FC/6-311G**	1.534 5	1.096 9	111.10
MP4 = Full/6-311G**	1.532 6	1.096 5	111.11

Optimization Level	S^2 B[a]	R C–C/Å	R C–H/Å	R C–H_2/Å	<CCH/deg	<CCH_2/deg
$C_2H_6^{+\bullet}$, ^2A_g $(C_{2h})_{DB}$						
MP2 = Full/6-31G** (ref. 3)	—	1.579	1.131	1.081	82.6	115.8
HF/6-311G**	Does not exist					
MP2 = Full/6-31G*	0.760	1.549 6	1.148 3	1.087 4	85.11	116.16
MP2 = Full/6-311G**	0.762	1.577 2	1.141 0	1.086 4	82.20	115.44
CID = FC/6-311G**	Does not exist					
CISD = FC/6-311G**	Does not exist					
CCD = FC/6-311G**	Does not exist					
ST4CCD = FC/6-311G**	0.764	1.663 0	1.127 1	1.089 3	81.51	112.86
QCISD = FC/6-311G**	0.765	1.735 8	1.112 3	1.087 8	82.77	110.14
QCISD(T) = FC/6-311G**	0.764	1.673 7	1.124 8	1.089 4	81.70	112.53
MP4 = FC/6-311G**	0.763	1.645 9	1.130 0	1.088 9	81.46	113.45

Optimization Level	S^2 B[a]	R C–C/Å	R C–H/Å	<CCH/deg
$C_2H_6^{+\bullet}$, $^2A_{1g}$ (D_{3d})				
HF/6-31G* (ref. 1)	—	1.976	1.076	98.4
MP2 = FC/6-31G* (ref. 1)	—	1.920	1.087	98.6
MP2 = Full/6-31G*	0.758	1.918 8	1.086 7	98.60
MP2 = Full/6-31G** (ref. 3)	—	1.918	1.082	98.3
HF/6-311G**	0.759	1.961 2	1.077 0	98.42
MP2 = Full/6-311G**	0.760	1.906 5	1.087 2	98.38
CID = FC/6-311G**	0.759	1.918 3	1.085 1	98.43
CISD = FC/6-311G**	0.759	1.917 2	1.085 4	98.42
CCD = FC/6-311G**	0.759	1.919 1	1.089 4	98.37
ST4CCD = FC/6-311G**	0.760	1.915 6	1.091 3	98.34
QCISD = FC/6-311G**	0.759	1.918 5	1.090 0	98.34

Table A.3 (*continued*)

Optimization Level[a]	S^2 B[a]	R C–C/Å	R C–H/Å	<CCH/deg
$C_2H_6^{+\bullet}$, $^2A_{1g}$ (D_{3d})				
QCISD(T) = FC/6-311G**	0.760	1.915 4	1.091 5	98.31
MP4 = FC/6-311G**	0.760	1.914 9	1.090 7	98.33
CASSCF(3,8)/6-31H*	—	1.972 6	1.075 9	98.56
CASSCF(5,7)/6-31G*	—	1.963 9	1.077 8	98.10

	Optimization level		
	MP2 = Full/6-311G**	HF/6-311G**	MP2 = Full/6-31G*
$C_2H_6^{+\bullet}$, $^2A''$ (C_s)			
S^2 B[a]	0.758	0.757	Does not exist
R C–C/Å	1.451 5	1.477 8	
R C–H/Å	1.085 8	1.076 7	
R C–H_2/Å	1.174 0	1.172 8	
R C–H′/Å[b]	1.086 9	1.080 0	
R C–H_2′/Å[b]	1.107 3	1.089 9	
<C–C–H/deg	122.89	123.24	
<C–C–H_2/deg	116.58	117.53	
<C–C–H′/deg[b]	114.74	113.05	
<C–C–H_2′/deg[b]	108.59	108.39	
Dihedral angle H–C–H[c]	70.5	67.1	
Dihedral angle H–C–H′[b,c]	110.0	115.0	
$C_2H_6^{+\bullet}$, ^2B_g (C_{2h})			
S^2 B[a]	0.770	0.770	0.766
R C–C/Å	1.436 1	1.423 8	1.436 6
R C–H/Å	1.085 9	1.076 4	1.086 9
R C–H_2/Å	1.139 6	1.137 1	1.139 9
<C–C–H/deg	118.51	118.65	117.84
<C–C–H_2/deg	112.24	112.13	112.08
Dihedral angle H–C–H[c]	91.7	92.3	96.8
$C_2H_6^{+\bullet}$, ^2A_g (C_{2h})[d]			
S^2 B[a]	0.772	Does not exist	Does not exist
R C–C/Å	1.444 7		
R C–H/Å	1.153 2		
R C–H_2/Å	1.103 9		
<C–C–H/deg	116.36		
<C–C–H_2/deg	113.64		
Dihedral angle H–C–H[c]	142.0		
Excited structures			
$C_2H_6^{+\bullet}$, ^2A_u (C_{2h})			
S^2 B[a]	0.760	0.761	0.757
R C–C/Å	1.618 6	1.584 2	1.617 4
R C–H/Å	1.087 9	1.077 4	1.088 5
R C–H_2/Å	1.137 2	1.137 2	1.136 8
<C–C–H/deg	113.63	114.49	113.29
<C–C–H_2/deg	114.68	114.77	114.56
Dihedral angle H–C–H[c]	99.5	99.9	101.7
^2B_g electronic energy (H/p)[e]	−79.157 55	−78.816 23	−79.059 72
$C_2H_6^{+\bullet}$, ^2B_u (C_{2h})			
S^2B[a]	0.762	0.761	0.759
R C–C/Å	1.616 3	1.582 6	1.615 6
R C–H/Å	1.159 1	1.169 3	1.158 7
R C–H_2/Å	1.102 7	1.093 7	1.102 7
<C–C–H/deg	116.27	115.83	116.01
<C–C–H_2/deg	113.43	114.10	113.26
Dihedral angle H–C–H[c]	138.3	138.5	137.1
^2A_g electronic energy (H/p)[e]	−79.155 04	−78.815 02	−79.057 57

[a] $\langle S^2 \rangle$ before annihilation of unwanted spin states; after annihilation $\langle S^2 \rangle$ was always 0.750. [b] Bond lengths and angles in the 'unperturbed' part of the molecule—see structure in the text. [c] Angle H–C–H in the corresponding Newman projection. [d] Not a true minimum—two negative frequencies. [e] Energy of the corresponding lowest 'vertical' (at the same geometry) state.